^{222}Rn and ^{220}Rn emanations as a function of the absorbed α-doses from select metamict minerals

REVISION 1

Dariusz Malczewski

Faculty of Earth Sciences, University of Silesia, Bedzinska 60, 41-200 Sosnowiec, Poland

e-mail: dariusz.malczewski@us.edu.pl

Maria Dziurowicz

Faculty of Earth Sciences, University of Silesia, Bedzinska 60, 41-200 Sosnowiec, Poland

e-mail: maria.dziurowicz@us.edu.pl

ABSTRACT

Metamict minerals contain uranium and thorium, which contribute to physical degradation or metamictization of their crystal structures over geologic time. The damage occurs primarily through progressive overlapping recoil nuclei collision cascades from α-decay of ^{238}U, ^{232}Th, ^{235}U and their daughter products. We measured ^{222}Rn and ^{220}Rn emanations from metamict samples of nine oxides (brannerite, davidite, fergusonites, pyrochlores, samarskites and uraninite), two phosphates (monazites), and eight silicates (cerite, gadolinites, perrierite, rinkite, thorite, turkestanite and vesuvianite). The total absorbed α-doses ranged from 1.4 x 10^{15} to 6.1 x 10^{18} α-decay mg^{-1} for cerite and uraninite, respectively. The ^{222}Rn emanation coefficients varied from 5 x 10^{-5}% (uraninite) to 2.5 % (turkestanite). The ^{220}Rn emanation coefficients varied from 7 x 10^{-3}% (gadolinite Ytterby) to 6.2% (gadolinite Marysin). The lowest ^{222}Rn emanation coefficients occurred among metamict minerals containing the highest concentrations of ^{238}U (i.e., uraninite, samarskites and brannerite). Overall, the ^{222}Rn and ^{220}Rn emanation coefficients observed in this study fall significantly below previously reported values.

INTRODUCTION

Metamict minerals develop from initially crystalline phases that experience physical damage to their crystal lattices due to the decay of radioactive elements. Metamictization (amorphization) is primarily caused by progressive overlapping nuclear recoil collision cascades from α-decay of ^{238}U, ^{232}Th, ^{235}U and their daughter products (Ewing et al. 2000). Age, as well as ^{238}U and ^{232}Th concentrations, determine the degree to which minerals undergo metamictization. The radon isotopes

1

35   ^{222}Rn ($T_{1/2}$ = 3.64 d) and ^{220}Rn (referred to as 'thoron', $T_{1/2}$ = 55.6 s) belong to the

36   ^{238}U and ^{232}Th decay series, and occur as inert gases that are detectable in U- and

37   Th-bearing mineral phases. The α-decay of ^{226}Ra (E_α = 4.77 MeV) is accompanied

38   by recoil of the ^{222}Rn nucleus with an energy of 86 keV. The α-decay of ^{224}Ra (E_α =

39   5.67 MeV) is accompanied by recoil of the ^{220}Rn nucleus with an energy of 103 keV.

40   The estimated direct recoil lengths of ^{222}Rn and ^{220}Rn within the relevant solid

41   materials typically range from 30 – 50 nm. Sakoda et al. (2010a) for example,

42   reported a ^{222}Rn recoil length of 34 nm for quartz (SiO_2).

43   Emanation coefficients (expressed in percentage) measure the number of

44   radon or thoron atoms released per the number of radon or thoron atoms produced

45   within the decay series for a given mineral. This ratio provides a quantitative measure

46   of the quality of the sample's internal structure. Six fundamental mechanisms have

47   been proposed to account for radon isotope emanations from solids. These include

48   direct recoil, diffusion through the material, indirect recoil, the knock-out effect,

49   penetrating recoil and radium distribution (Semkov 1990, 1991; Morawska and

50   Phillips 1992). Moisture content and grain size also affect radon emanations from

51   these phases (Semkov 1991; Barillon et al. 2005; Sakoda et al. 2010a). The ^{222}Rn

52   emanation coefficients reported for rock forming minerals and certain rock

53   compositions typically range from about 1% to 25% (Krishnaswani and Seidemann,

54   1988; Sakoda et al. 2011). Extremely high emanation coefficients (~40%) were

55   reported for minerals associated with weathered granitic soil (Sakoda et al. 2010b).

56   Literature sources have often used different mineral preparation methods to

57   analyze emanations and thus report inconsistent results. Systematic studies that

58   were strictly devoted to five metamict minerals crushed to grain sizes ranged from 63

59   to 2000 μm, were done by Garver and Baskaran (2004). The results obtained in that

60   work and those reported by Landa (1987) for three types of uranium ores are given in

61   Tab. 1. Table 1 lists previously reported radon emanation coefficients for metamict

62   minerals, ranging from 0.53% (uraninite) to 17% (cerite). The mass emanation rates

63   varied from 10 to 1860 atoms g^{-1} min^{-1} for monazite and uraninite, respectively.

64   Estimated radon emanation coefficients for uranium ores ranged between 2%

65   (autunite) to 19% (carnotite).

66   The purpose of this work is to determine the relationship between ^{222}Rn and

67   ^{220}Rn emanations and absorbed α-doses for a representative group of metamict

2

68 minerals. This paper provides experimental data concerning ^{222}Rn and ^{220}Rn

69 emanations for metamict oxides, silicates and phosphates.

70

71 **MATERIALS and METHODS**

72   Nineteen samples of metamict minerals were collected from many different

73 global locations. Table 2 lists basic physical characteristics and ages of samples

74 analyzed. The surface area of each mineral was accurately determined and the

75 projecting method was used to calculate it. Each mineral face was carefully projected

76 onto graph paper. The squared meshes were added up. All of the larger irregularities

77 such as cracks, concavity or convexity were taken into account. Quantitative

78 measurements of the smallest irregularities were not feasible. The surface emanation

79 rates presented here should thus be regarded as the upper limits of emanations.

80 The samples differ in terms of mass and surface area (e.g., m = 0.242 g and S = 1.82

81 cm^2 for turkestanite, to m = 160.595 g and S = 62.29 cm^2 for uraninite), and range in

82 age from 270 Ma (davidite) to 2660 Ma (fergusonite Mukinbudin). Mineral samples

83 were analyzed for their X-ray diffraction (XRD) patterns using a PHILIPS X'Pert

84 diffractometer in the Θ-Θ system and CuKα radiation in scan mode with step size of

85 0.02^o. Sample XRD patterns are shown in Figure 1.

86   The activity concentrations of ^{238}U and ^{232}Th were determined for each mineral

87 based on the gamma-ray activities of ^{214}Pb and ^{214}Bi (^{238}U), and ^{228}Ac (^{232}Th). The

88 activity concentrations of ^{235}U were calculated based on the natural abundance of

89 ^{238}U/^{235}U = 137.88. The activities of the radionuclides were calculated from the

90 following gamma transitions (energy in keV): ^{214}Pb (242.9, 295.2 and 351.9), ^{214}Bi

91 (609.3, 786.3, 1120.3 and 1764.5) and ^{228}Ac (338.3, 911.6, 964.5 and 969.1)

92   Gamma-ray spectra were recorded using a GX3020 system consisting of a

93 coaxial HPGe detector (32% efficiency, crystal length 59 mm and diameter 56.6 mm)

94 in a lead and copper shield (60 mm) with a multichannel buffer (InSpector 2000

95 DSP). The detector bias voltage was 4000 V and the energy resolution was 0.8 keV

96 at 122 keV and 1.7 keV at 1.33 MeV. Two software packages were used for the

97 efficiency calibration and the determination of radionuclides: LabSOCS (Laboratory

98 Sourceless Calibration Software) and Genie 2000 v.3. The total duration of a single

99 measurement varied from about 3 to 7 days. Since γ-emitters in both uranium series

100 (^{234m}Pa → ^{226}Ra → ^{214}Pb → ^{214}Bi) and thorium series (^{228}Ac → ^{224}Ra → ^{212}Pb → ^{212}Bi

101 → ^{208}Tl) were found in radioactive equilibrium for each mineral, we assumed that

3

102   activity concentrations of ^{222}Rn and ^{220}Rn were the same as those for ^{238}U and ^{232}Th.

103   The ^{238}U activity concentrations for these minerals exhibit an extremely wide range

104   from 0.36 Bqg^{-1} (cerite) to 9465 Bqg^{-1} (uraninite). The ^{232}Th activity concentrations for

105   these minerals range from 5.1 Bqg^{-1} (uraninite) to 1054 Bqg^{-1} (thorite). These activity

106   concentrations corresponded to a calculated total absorbed α-dose range of 1.36 x

107   10^{15} α-decay mg^{-1} (cerite) to 6.09 x 10^{18} α-decay mg^{-1} (uraninite). Table 3 lists the

108   integrated α-doses for each of the mineral samples analyzed.

109   We used a RAD7 radon system (Durridge Company, Inc.) to measure

110   ^{222}Rn and ^{220}Rn emanations. The system contains a solid-state ion-implanted planar

111   silicon detector and a built-in pump with a flow rate of 1 Lmin^{-1}. It has a desiccant

112   (CaSO$_4$) unit and inlet filters (pore size 1 μm). The RAD7's internal sample cell is a

113   0.7 L conducting hemisphere with a 2200 V potential relative to the detector that is

114   placed at the center of the hemisphere. The detector operates in internal humidities

115   of 0% to 10% with a sensitivity of 4 Bqm^{-3} and an upper linear detection limit of 800

116   kBqm^{-3} (8 MBqm^{-3} using additional extender). The detector was manufactured with a

117   calibration accuracy of ± 5%. The spectra are in 200 channels and grouped into 8

118   windows of energy ranges. A, B, C, and D are the major windows and E, F, G and H

119   are the diagnostic windows. Window A covers the energy range from 5.40 to 6.40

120   MeV, showing the total counts from 6.00 MeV α particles from the 3-minute ^{218}Po

121   decay (daughter of ^{222}Rn). Window B covers the region 6.40 MeV to 7.40 MeV,

122   showing the total counts of the 6.78 MeV α particles from the 0.15-second ^{216}Po

123   (^{220}Rn daughter). Window C represents the total counts of the 7.69 MeV α particles

124   from ^{214}Po (the fourth nuclide in the ^{222}Rn decay chain), while window D represents

125   the total counts of the 8.78 MeV α particles from the decay of ^{212}Po (the fourth

126   nuclide in the ^{220}Rn decay chain). The measurements presented here were carried

127   out in sniff mode. Sniff mode means that the RAD7 calculates ^{222}Rn concentrations

128   from the data in window A only and ^{220}Rn concentrations from the data in window B,

129   while the data from windows C and D are ignored. In this mode, the built-in pump

130   runs continuously. The mineral sample was placed in a stainless steel cylinder (ϕ = 8

131   cm, h = 3 cm) with two inlets on opposing sides. Following sample insertion, the

132   cylinder was firmly affixed and the inlets were connected to a desiccant chamber and

133   to the RAD7 inlet (Fig. 2). The drying unit remained open to the ambient environment

134   (open loop mode). Measurements consisted of a 15 minute analysis repeated over

4

135   ten cycles for a 150 minute run time. Tabulated results represent the average of
136   these three measurement runs. Temperatures ranged from 21 - 23 $^{\circ}$C during
137   analytical runs and external relative humidity ranged from 13 - 15%. The ambient
138   ^{222}Rn background level ranged from 4.6 to 6.8 Bqm^{-3}, whereas ^{220}Rn background
139   levels fell below detection limits. Radiometric measurements were performed at the
140   Laboratory of Natural Radioactivity (Faculty of Earth Sciences, University of Silesia).

141   Total emission rates for ^{222}Rn (E$_{222}$) and ^{220}Rn (E$_{220}$) from the mineral samples
142   were calculated in atoms s^{-1} according to the following equations:

143
$$E_{222} = \frac{C_{222} \cdot v}{6 \cdot 10^4 \cdot \lambda_{222}}$$

144   and

145
$$E_{220} = \frac{1.28 \cdot C_{220} \cdot v}{6 \cdot 10^4 \cdot \lambda_{220}}$$

146   where C$_{222}$, C$_{220}$ are the ^{222}Rn and ^{220}Rn concentrations minus ambient
147   concentrations (Bqm^{-3}); v = 1 Lmin^{-1} is the flow rate; λ_{222} = 2.1 x 10^{-6} s^{-1} and λ_{220} =
148   0.012 s^{-1} are the decay constants of ^{222}Rn and ^{220}Rn. Our experimental set-up (Fig.
149   2) included a 20 s delay between emission and measurement by the RAD7 unit. The
150   C$_{220}$ term is therefore multiplied by 1.28. The mass and surface emanation rates of
151   ^{222}Rn and ^{220}Rn for each mineral were calculated as:

152
$$e_{m222} = \frac{E_{222}}{m} \, , \ \ e_{s222} = \frac{E_{222}}{S}$$

153   and

154
$$e_{m220} = \frac{E_{220}}{m} \, , \ \ e_{s220} = \frac{E_{220}}{S}$$

155   where e$_{m222}$ and e$_{m220}$ are the respective ^{222}Rn and ^{220}Rn mass emanation rates,
156   e$_{s222}$ and e$_{s220}$ are the surface emanation rates of ^{222}Rn and ^{220}Rn, and m and S
157   respectively refer to the mass and the surface area of the sample.

158   The surface area of each mineral was accurately determined but quantitative
159   measurements of cracks and irregularities were not feasible. Surface emanation
160   rates presented here should thus be regarded as upper limits of emanations. The

5

161   ^{222}Rn and ^{220}Rn emanation coefficients (e_{222} and e_{220}, respectively) were calculated

162   as the ratio of the ^{222}Rn and ^{220}Rn atoms emitted from a mineral (min^{-1}) and the total

163   amount of ^{222}Rn and ^{220}Rn produced inside the mineral:

164    $$e_{222} = \frac{E_{222}}{N_{222}}$$

165   and

166    $$e_{220} = \frac{E_{220}}{N_{220}}$$

167   where N_{222} and N_{220} represent the production rate (atom s^{-1}) of ^{222}Rn and ^{220}Rn

168   nuclei in the samples, assuming radioactive equilibrium conditions within the ^{238}U and

169   ^{232}Th decay series. In these equations E_{222} and E_{220} are expressed in atom min^{-1} in

170   order to compare e_{222} and e_{220} with the results reported by Garver and Baskaran

171   (2004).

172   **RESULTS**

173   Table 4 lists emissions, mass and surface emanation rates, and calculated

174   ^{222}Rn and ^{220}Rn emanation coefficients for all 19 samples. Tables 5 and 6 list

175   correlation matrix values for ^{222}Rn and ^{220}Rn emanations, and other calculated

176   variables for metamict oxides and silicates, respectively.

177   As shown in Table 4 and Figure 3, turkestanite, cerite, monazite Petaca and

178   thorite gave the highest e_{222} values. Uraninite, samarskites and fergusonite

179   Madawaska gave the lowest e_{222} values. The ^{222}Rn emanation coefficients varied

180   over five orders of magnitude from 4.9 x 10^{-5} % (uraninite) to 2.49 % (turkestanite).

181   Gadolinite Marysin, thorite, turkestanite and rinkite gave the highest e_{220}

182   values for ^{220}Rn, whereas gadolinite Ytterby, samarskite Centennial Cone, uraninite

183   and vesuvianite gave the lowest e_{220} values (Fig. 4). The ^{220}Rn emanation

184   coefficients varied within three orders of magnitude from 0.007% in gadolinite Ytterby

185   to 6.24% in gadolinite Marysin. This latter sample represents an intermediate state

186   between a highly metamict and crystalline morphology for gadolinite, and was also

187   subjected to hydrothermal alteration over geological time (Janeczek and Eby 1993).

6

188   The calculated ^{222}Rn mass emanation rates (e_{m222}) ranged from 3 to 2910

189   atoms g^{-1} s^{-1} (Fig. 5a, Table 4). Samples THO, MPE and TUR gave the highest e_{m222}

190   values (2910 - 1540 atoms g^{-1} s^{-1}), whereas samples GYT, SCC and MBU gave the

191   lowest values (3 - 15 atoms g^{-1} s^{-1}; Fig. 5a). The ^{222}Rn (e_{s222}) surface emanation

192   rates varied from 2 to 1460 atoms cm^{-2} s^{-1} (Fig. 5b). Samples MPE, THO and TUR

193   gave the highest e_{s222} values (1460 - 207 atoms cm^{-2} s^{-1}) whereas samples GYT,

194   SCC and CER gave the lowest values (2 - 9 atoms cm^{-2} s^{-1}). The majority of e_{m222}

195   (12) and e_{s222} (13) observations fell within the range of 10-100 atoms g^{-1} s^{-1} or atoms

196   cm^{-2} s^{-1} (respectively). Three samples exhibited values for e_{m222} in excess of 1000

197   atoms g^{-1} s^{-1} and two samples gave mass emanations below 10 atoms g^{-1} s^{-1}.

198   Conversely, two samples gave e_{s222} in excess of 1000 atoms cm^{-2} s^{-1} and three

199   samples gave surface emanations below 10 atoms cm^{-2} s^{-1} (Fig. 5a and b).

200   As expected, ^{220}Rn emanation rates fell below those observed for ^{222}Rn (Fig.

201   6a and b). The calculated ^{220}Rn mass emanation rates (e_{m220}) ranged from 0.001 to

202   79 atoms g^{-1} s^{-1} (Fig. 6a). Similar to ^{222}Rn, samples THO, MPE and TUR gave the

203   highest e_{m220} values (79 - 12 atoms g^{-1} s^{-1}). Samples GYT, URA and VES gave the

204   lowest e_{m220} values (0.001 - 0.02 atom g^{-1} s^{-1}). The calculated ^{220}Rn surface

205   emanation rates (e_{s220}) varied from 8 x 10^{-4} to 38 atoms cm^{-2} s^{-1} (Fig 6b). Samples

206   THO, MPE and TUR again gave the highest e_{s220} values (38 - 2 atoms cm^{-2} s^{-1}) and

207   samples GYT, VES and URA gave the lowest ^{220}Rn surface emanations (8 x 10^{-4} -

208   0.013 atom cm^{-2} s^{-1}) (Fig. 6b). The majority of both e_{m220} (11) and e_{s220} (14)

209   observations fell within the ranges of 0.01 to 1 atom g^{-1} s^{-1} and atom cm^{-2} s^{-1},

210   respectively. In the case of e_{m220}, six observations fell within the 1 to 100 atoms g^{-1} s^{-1}

211    $^{-1}$ range whereas three observations fell within the 1 to 100 atoms cm^{-2} s^{-1} range for

212   e_{s220}. As shown in Figure 6a and 6b, two observations for both e_{m220} and e_{s220} fell

213   below 0.001 atom g^{-1} s^{-1} and atom cm^{-2} s^{-1}, respectively.

214   **Correlations**

215   Oxides

216   Table 5 shows that the total α-dose, D_T, and D_{238} are perfectly correlated (D_T -

217   D_{238}, r = 1), whereas D_T and D_{232} are uncorrelated (D_T - D_{232}, r = 0.03) for metamict

218   oxides. This indicates that α-decay within the ^{238}U series provides the dominant

219   contribution to the total α-dose, evident in similar relationships between the D_T and

7

220   D_{238} parameters for other mineral classes within the sample suite. The ^{222}Rn mass

221   emanation rates (e_{m222}) show a significant correlation with ^{232}Th series α-dose (e_{m222}

222   - D_{232}, r = 0.87). The highest coefficient associated with e_{s222} exists between D_{238} and

223   D_T (r = 0.92). The e_{m220} and D_{232} parameters also had a higher correlation coefficient

224   (r = 0.94), which contrasts with the weaker relationship observed between e_{s220} and

225   D_{232} (r = 0.69). Values for e_{220} exhibited a noteworthy negative correlation with D_{238} (-

226   0.46) and D_{232} (-0.25). For metamict oxides, the e_{222} and e_{220} emanation coefficients

227   exhibit strong correlation (r = 0.85). The ^{220}Rn emanation correlates with e_{222} but not

228   with e_{m222}, e_{m220} and e_{s220} (Table 5).

229
230   Silicates

231   As shown in Table 6 for metamict silicates, the total α-dose, D_T, perfectly

232   correlates with D_{238} and D_{232} (r = 0.99 and 1, respectively). This indicates that the

233   total absorbed α-dose is equally distributed between D_{238} and D_{232}. The strong

234   relationship between D_{238} and D_{232} (r = 0.99) indicates that these doses contribute

235   the same degree of α-dose in the samples examined. The emanation rates e_{m222},

236   e_{s222}, e_{m220} and e_{s220} correlate strongly with D_T, and have r values ranging from 0.9 to

237   1.0. In contrast to those of oxide samples, the e_{222} and e_{220} emanation coefficients for

238   metamict silicates do not correlate (r = -0.02). Mass and surface emanations for both

239   ^{222}Rn and ^{220}Rn showed a high degree of correlation, evident as r values of 0.94

240   (e_{m222} -e_{m220}) and 1 (e_{s222} - e_{m220}). The e_{s222} showed a weak correlation with e_{m222} (r =

241   0.38). Correlation coefficients between e_{220} and parameters other than e_{222} varied

242   within the narrow range of 0.52 (e_{220}-D_{238}) to 0.57 (e_{220}-e_{s222} and e_{220}-e_{m220}) (Table 6).

243
244   **DISCUSSION**

245   Emanation coefficients for ^{222}Rn generally decrease with increasing total α-

246   dose, D_T (Fig. 3 and Table 4). Metamict oxides showed the lowest ^{222}Rn emanation

247   coefficients for the highest absorbed α-dose. The oxide samples with a total dose D_T

248   < 10^{17} for α-decay mg^{-1} (DAV, PDF and PLF) generally exhibited higher emanation

249   coefficients than oxides with the highest D_T. Surprisingly, among the silicate samples,

250   the fully metamict gadolinite from Ytterby showed the lowest e_{222} values (10^{-4}%).

251   Oxides consist of close packed, ionically bonded structures that typically have fewer

252   cation sites than those available in silicate phases, which are characterized by more

253   open and complex lattice structure (Ewing and Haaker 1980). A uraninite sample

8

254 gave the lowest emanation coefficient (10^{-5}%) in spite of having the highest ^{238}U

255 concentrations and absorbed α-dose. Among the minerals analyzed, uraninite has

256 the simplest structure and chemical composition. The structure of the URA sample

257 shows a significant degree of crystallinity (long range order). The condition of the

258 sample and its compact structure explain the apparently independent relationship

259 between emanation coefficients and α-dose observations. The structure of uraninite

260 is also practically dose independent due to its high rate of self-annealing process

261 (Janeczek et al. 1996). Wang et al. (1998) observed similar patterns among simple

262 oxides phases irradiated by ion beams.

263 With the exception of the brannerite sample (BRA), the oxide samples exhibiting the

264 lowest e_{222} values (SCC, SRM and FMA) were completely metamict. Vitrification

265 resulting from the metamictization process can occlude void spaces in the structure

266 and thus hinder gas permeability in altered samples.

267 The e_{222} values for cerite, monazite, uraninite and thorite resemble those

268 reported by Garver and Baskaran (1993). Their research reported an e_{222} value of

269 0.98% for a monazite Petaca, which resembled the 0.73% value reported here for a

270 similar sample. Garver and Baskaran (1993) also reported emanation coefficients of

271 17 - 23%, 0.53%, and 5.38% for cerite, uraninite and thorite, respectively. Their

272 coefficients are markedly higher than those reported here (0.79%, 4.9 x 10^{-5}% and

273 0.30% for cerite, uraninite and thorite, respectively). Landa (1987) reported

274 significantly higher e_{222} values for uranium-bearing minerals, autunite (2 - 4%),

275 carnotite (12 - 19%), and uraninite (12 - 15%; Table 1).

276 Figure 3 shows that ^{222}Rn emanations produce visible peaks for metamict

277 phases having ^{232}Th concentrations in excess of 2.8 wt.% and $D_{232} > 26$ x 10^{15} α-

278 decay mg^{-1} (TUR, FMA, BRA, MPE, and THO; Tables 2 and 3). Excluding these

279 observations, the relationship between e_{222} and total dose (D_T) values can be fitted

280 by the exponential function:

281 $$e_{222}(\%) = a_0 + a_1 \exp(-D_T b_1) + a_2 \exp(-D_T b_2) + a_3 \exp(-D_T b_3)$$

282 where $a_0 = 5.14$ x 10^{-5}, $a_1 = 1.63$ x 10^{-3}, $a_2 = 0.29$, $a_3 = 6.82$, $b_1 = 5.83$ x 10^{-18}, $b_2 =$

283 4.96 x 10^{-16} and $b_3 = 1.78$ x 10^{-15}.

284 Sample SRM was the only evident outlier relative to the fitted curve. For $D_T <$

285 10^{15} α-decay mg^{-1}, e_{222} approaches 7.1%, and for $D_T > 10^{19}$ α-decay mg^{-1}, e_{222}

286 behaves as a constant equal to 5.14 x 10^{-5} %.

9

287   Samples TUR, MPE, THO, FMU and BRA form a distinct group deviating from

288   the fitted relationship, and justifying their exclusion from it. The weighted average

289   energy of recoil nuclei in the ^{232}Th and ^{238}U decay series explains their variation

290   relative to other samples. The weighted average α particle energy of 6.18 MeV, and

291   the weighted average energy of recoil nuclei of 114 keV were calculated for the ^{232}Th

292   decay series using standard nuclide reference sources (Firestone, 1996). These

293   values exceed those for the ^{238}U decay series (5.34 MeV and 98 keV, respectively).

294   Recoil nuclei from the ^{232}Th decay series can therefore potentially cause greater

295   radiation damage than those from the ^{238}U series, creating linked microcracks that

296   penetrate the mineral structure more deeply than is possible given the direct recoil

297   length of ^{222}Rn and ^{220}Rn (i.e., ~ 40 nm).

298   The impact of α-decay from the ^{232}Th series is particularly evident in mass and

299   surface emission rates (Fig. 5 and 6). Silicate samples with the highest ^{232}Th

300   concentrations (THO, MPE and TUR) gave the highest values both for ^{220}Rn and

301   ^{222}Rn mass and surface emission rates. The effect of ^{232}Th series α-decay on ^{222}Rn

302   emanations also appears to influence metamict oxides, contributing to an e_{m222} - D_{232}

303   correlation coefficient of 0.87. This indicates that both the surface (e_{s222} − D_{238}, r =

304   0.92) and deeper layers of the minerals contribute to ^{222}Rn emanations as a result of

305   ^{232}Th series α-decays.

306   Unlike ^{222}Rn, the ^{220}Rn emanation coefficients were apparently independent of

307   D_T for all of the investigated minerals (Fig. 4). Samples with the most glassy

308   appearance (gadolinite from Ytterby and samarskite from the Centennial Cone)

309   exhibited the lowest e_{220} values ($7 \cdot 10^{-3}$ and 0.02%, respectively). For other minerals,

310   e_{220} values varied within a relatively narrow range of 0.1 - 10% (Fig. 4).

311   Two significant differences exist between metamict oxides and silicates with

312   respect to ^{222}Rn and ^{220}Rn emanations. For metamict oxides, ^{220}Rn emanation

313   coefficients are about two orders of magnitude higher than ^{222}Rn emanations (Fig.

314   8a). This observation likely arises from the lower production rate of ^{220}Rn atoms

315   relative to ^{222}Rn atoms (3-4 orders of magnitude) in uranium-rich oxides. Closed

316   system behavior of ^{220}Rn leads to a relatively high ratio of ^{220}Rn$_{escaped}$ relative to total

317   ^{220}Rn within the sample (Eq. 3). Semkov (1991) reported an empirically derived

318   e_{220}/e_{222} ratio of 1.84 for pitchblende. This ratio, 1.84, was explained by ^{220}Rn's

319   broader physical range relative to ^{222}Rn, which allows the former to penetrate surface

320   irregularities to a greater degree, thus producing more emanation channels. Among

321   metamict silicates, e_{222} and e_{220} values are comparable but uncorrelated (Fig. 8b).

322   The two samples of monazites analyzed differed markedly in terms of their ^{222}Rn and

323   ^{220}Rn emanations. The partially metamict MPE sample exhibited an e_{222} value about

324   three times higher and an e_{220} value about 15 times higher than those of MBU, a

325   highly crystalline sample with few irregularities. Mass and surface emission rates for

326   MPE were also much higher than those of MBU (Fig. 5 and 6). These differences

327   may arise from the significant age differences and   thorium and uranium

328   concentrations between the two samples. Consequently, the total absorbed α-dose in

329   MPE exceeds that of MBU by about two orders of magnitude. Gadolinites exhibited

330   the opposite trend wherein the fully metamict GYT sample showed definitely lower

331   e_{222} and e_{220} values than those observed for the partially metamict GMA sample.

332   Different oxide samples of the same mineral phase (PDF and PLF; SCC and SRM)

333   subjected to comparable absorbed α-doses, for example, exhibited similar emanation

334   coefficients (Fig. 3). The emanation properties of thorium-rich minerals having

335   varying degrees of metamictization require further analysis and interpretation.

336   For the most part, the emanation results presented here can be explained by

337   Semkov's (1991) fractal model of radon emanation from solids. The model

338   emphasizes the salient effects of the fractal dimensions of the mineral surface on

339   radon emanations. A comprehensive model of ^{222}Rn and ^{220}Rn emanations from

340   metamict minerals should also consider the internal transport of ^{222}Rn and ^{220}Rn

341   within microcracks. This mechanism seems to be especially important for silicates

342   with high concentrations of Th.

343

344   **IMPLICATIONS**

345   Changes in the emanation coefficients and emanation rates of ^{222}Rn and ^{220}Rn

346   for metamict minerals are significant for assessing open- and closed- system

347   behavior for minerals whose internal structure is affected by α-decay in the ^{238}U,

348   ^{232}Th and ^{235}U decay series. These constraints on alteration can thus help to

349   determine which minerals are suitable analytical targets for Pb/U and Th

350   geochronology. The results presented here can also help to assess the material

351   suitability for high-level nuclear waste (HLW) forms.

352

353   **ACKNOWLEDGMENTS**

11

356
357
358

359   **REFERENCES**

360

361   Barillon, R., Özgümüs, A., and Chambaudet, A. (2005) Direct recoil radon emanation
362   from crystalline phase. Influence of moisture content. Geochimica et Cosmochimica
363   Acta, 69, 2735-2744.

364

365   Blight, D.F., Chin, R.J., and Smith, R.A. (1984) 1:250 000 map sheet, Geological
366   Series, Explanatory Notes, Geological Survey of Western Australia.

367

368   Bryant, B., McGrew, L.W., and Wobus, R.A. (1981) Geologic map of the Denver 1 x 2
369   degree quadrangle, north-central Colorado: U.S. Geological Survey Miscellaneous
370   Investigations Map I-1163, scale 1:250,000.

371

372   Carr, S.D., Easton, R.M., Jamieson, R.A., and Culshaw, N.G. (2000) Geologic
373   transect across the Grenville Orogen of Ontario and New York. Canadian Journal of
374   Earth Sciences, 37, 193-216.

375

376   Easton, R.M. (1992) The Grenville Province. In Geology of Ontario. Chapter 19,
377   Ontario Geological Survey, Special Volume 4, Part 2, 713-904.

378

379   Ewing, R.C., and Haaker, R.F. (1980) The metamict state: implications for radiation
380   damage in crystalline waste form. Nuclear and Chemical Waste Management, 1, 51-
381   57.

382

383   Ewing, R.C., Meldrum, A., Wang, L.M., and Wang S.X. (2000) Radiation-induced
384   amorphization. In Redfern, S.A.T., and Carpenter, M.A. (eds) Reviews in Mineralogy
385   and Geochemistry, 39, 319-361.

386

387   Firestone, R.B. (ed) (1996) Table of isotopes. Wiley-Interscience, Lawrence Berkeley
388   National Laboratory.

389

390   Garver, E., and Baskaran, M. (2004) Effects of heating on the emanation rates of
391   radon-222 from a suite of natural minerals. Applied Radiation and Isotopes, 61, 1477-
392   1485.

393

394   Janeczek, J., and Eby, R.K. (1993) Annealing of radiation damage in allanite and
395   gadolinite. Physics and Chemistry of Minerals, 19, 343-356.

396

397   Janeczek, J., Ewing, R.C., Oversby, V.M., and Werme, L.O. (1996) Uraninite and
398   UO_2 in spent nuclear fuel: a comparison. Journal of Nuclear Materials, 238, 121-130.

399

400   Kabalov, Yu.K., Sokolova, E.V., Pautov, L.A., and Schneider, J. (1998) Crystal
401   structure of a new mineral turkestanite: a calcium analogue of steacyite.
402   Crystallography Reports, 43, 584-588.

403

404   Krishnaswami, S., and Seidemann, D.E. (1988) Comparative study of ^{222}Rn, ^{40}Ar,
405   ^{39}Ar and ^{37}Ar leakage from rocks and minerals: implications for the role of nanopores
406   in gas transport through natural silicates. Geochimica et Cosmochimica Acta, 52,
407   655-658.

408

409   Landa, E.R. (1987) Influence of ore type and milling procession ^{222}Rn emanation
410   coefficients of U mill tailings. Health Physics, 53, 679-683.

411

412   Leech, M.L., and Stockli, D.F. (2000) The late exhumation history of the ultrahigh-
413   pressure Maksyutov Complex, south Ural Mountains, from new apatite fission track
414   data. Tectonics, 19, 153-167.

415

416   Ludwig, K.R., and Cooper, J.A. (1984) Geochronology of Precambrian granites and
417   associated U-Ti-Th mineralisation, northern Olary province, South Australia.
418   Contributions to Mineralogy and Petrology, 86, 298-308.

419

420   Lumpkin, G.R., and Ewing, R.C. (1988) Alpha-decay damage in minerals of the
421   pyrochlore group. Physics and Chemistry of Minerals, 16, 2-20.

422

423   Morawska, L., and Phillips, C.R. (1993) Dependence of the radon emanation
424   coefficient on radium distribution and internal structure of the material. Geochimica et
425   Cosmochimica Acta, 57, 1783-1797.

426

427   Pin, H., Mierzejewski, M.P., and Duthou, J.L. (1987) Age of Karkonosze Mts. Granite
428   dated by isochrome Rb/Sr and its initial 87Sr/86Sr value. Przegląd Geologiczny, 10,
429   512-517 (in Polish).

430

431   Reznitskii, L.Z., Kotov, A.B., Sal'nikova, E.B., Vasil'ev, E.P., Yakovleva, S.Z., Kovach,
432   V.P., and Fedoseenko, A.M. (2000) The Age and Time Span of the Origin of
433   Phlogopite and Lazurite Deposits in the Southwestern Baikal Area: U-Pb
434   Geochronology. Petrology, 8, 74-86 (in Russian).

435

436   Romer, R.L., and Smeds, S.A. (1994) Implications of U-Pb ages of columbite-
437   tantalites from granitic pegmatites for the Palaeoproterozoic accretion of 1.90-1.85
438   Ga magmatic arcs to the Baltic Shield. Precambrian Research, 67, 141-158.

439

440   Sakoda, A., Hanamoto, K., Ishimori, Y., Kataoka, T., Kawabe, A., and Yamaoka, K.
441   (2010a) First model of the effect of grain size on radon emanation. Applied Radiation
442   and Isotopes, 68, 1169-1172.

443

444   Sakoda, A., Ishimori, Y., and Yamaoka, K. (2011) A comprehensive review of radon
445   emanation measurements for mineral, rock, soil, mill tailing and fly ash. Applied
446   Radiation and Isotopes, 69, 1422-1435.

447

448   Sakoda, A., Nishiyama, Y., Hanamoto, K., Ishimori, Y., Yamamoto, Y., Kataoka, T.,
449   Kawabe, A., and Yamaoka, K. (2010b) Differences of natural radioactivity and radon
450   emanation fraction among constituent minerals of rock or soil. Applied Radiation and
451   Isotopes, 68, 1180-1184.

452

13

453   Semkow, T.M. (1990) Recoil-emanation theory applied to radon release from mineral
454   grains. Geochimica et Cosmochimica Acta, 54, 425-440.
455
456   Semkow, T.M. (1991) Fractal model of radon emanation from solids. Physical Review
457   Letters, 66, 3012–3015.
458
459   Wang, S.X., Wang, L.M., Ewing, RC., and Doremus, RH. (1998) Ion beam-induced
460   amorphization in MgO-Al$_2$O$_3$-SiO$_2$. I. Experimental and theoretical basis. Journal of
461   Non-Crystalline Solids, 238, 198-213.

462
463
464   **FIGURE CAPTIONS**
465
466   **FIGURE 1.**

467   X-ray diffraction (XRD) patterns of mineral samples analyzed for radon emanations.

468   **FIGURE 2.**

469   Experimental apparatus for measuring ^{222}Rn and ^{220}Rn emanations.

470   **FIGURE 3.**

471   ^{222}Rn emanation coefficients (e_{222}) for metamict samples vs. total absorbed α-dose.

472   **FIGURE 4.**

473   ^{220}Rn emanation coefficients (e_{220}) for metamict samples vs. total absorbed α-dose.

474   **FIGURE 5.**

475   **(a)** Mass (e_{m222}) and **(b)** surface (e_{s222}) ^{222}Rn emanation rates for metamict samples
476   analyzed. Estimates of ^{222}Rn atoms emitted are noted above bars for each sample.

477   **FIGURE 6.**

478   **(a)** Mass (e_{m220}) and **(b)** surface (e_{s220}) ^{220}Rn emanation rates for metamict samples
479   analyzed. Estimates of ^{220}Rn atoms emitted are noted above bars for each sample.
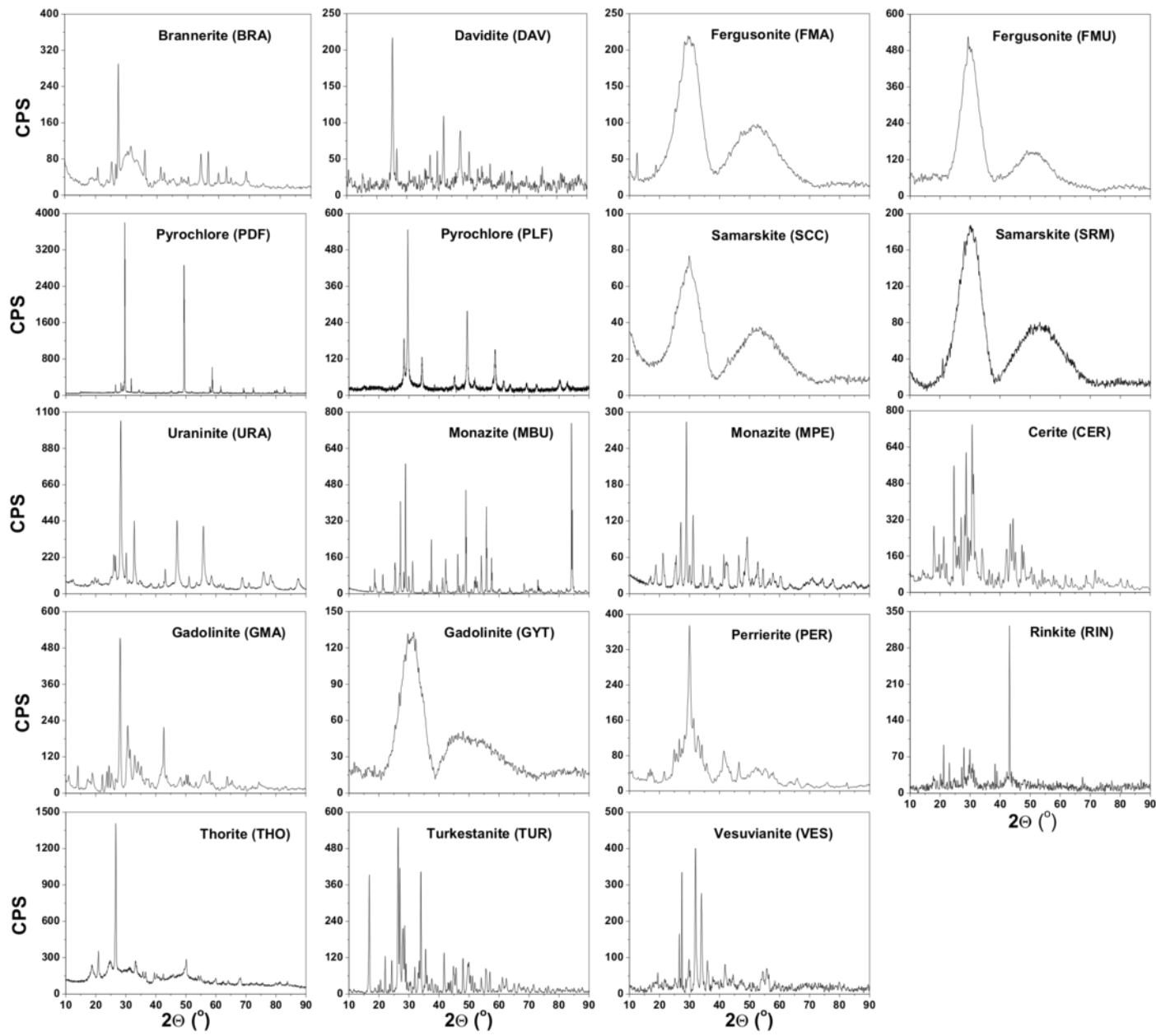
480   **FIGURE 7.**

481   Emanation coefficients for ^{222}Rn vs. total absorbed α-dose, excluding samples BRA,
482   FMU, MPE, THO and TUR. The solid line represents fitted exponential function
483   described by Eq. 4.The multiple regression coefficient is 0.74.

484   **FIGURE 8.**

485   Comparison of **(a)** e_{222} vs. absorbed total α-dose for metamict oxides and **(b)** e_{220} vs.
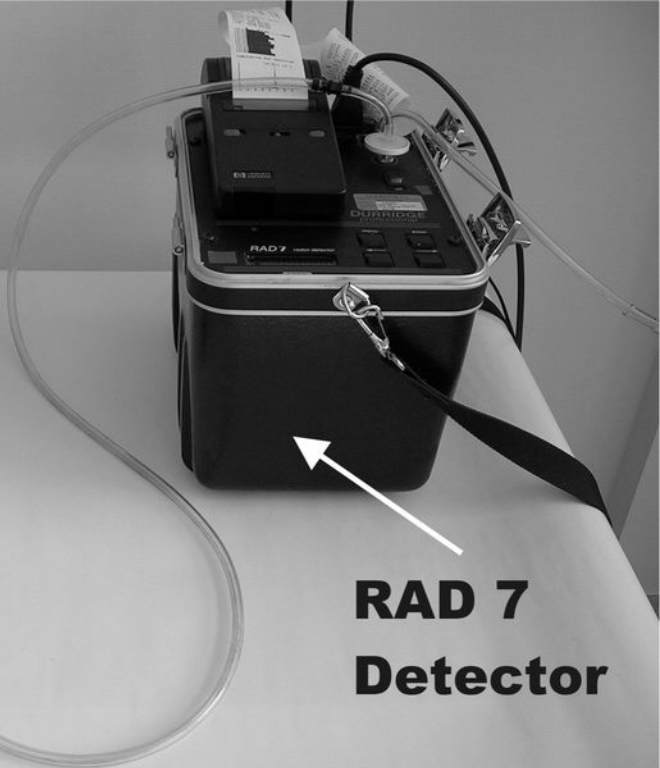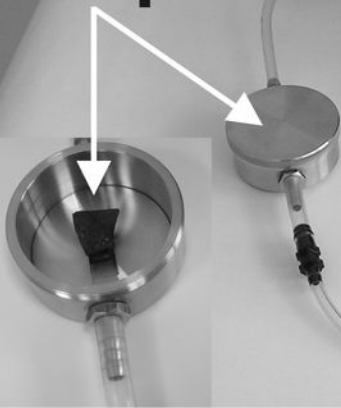486   absorbed total α-dose for metamict silicates.   ● ^{222}Rn;   ■ ^{220}Rn.
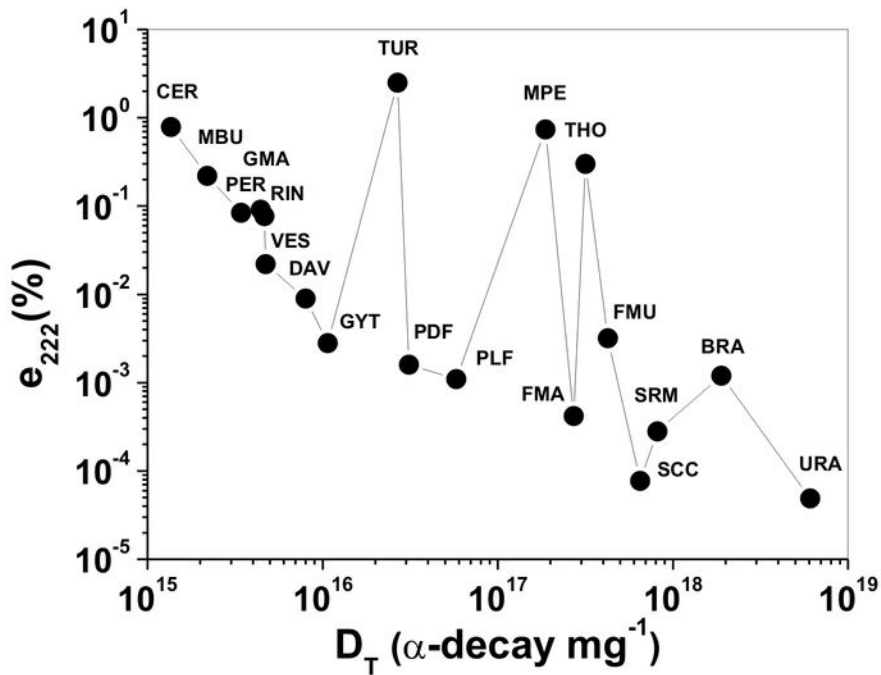
487

14

(a)

e_{m222} (atom g^{-1} s^{-1})

2910 1560 1540 360 227 99 74 72 55 53 47 39 37 28 23 23 13 8 3

THO MPE TUR BRA GMA FMU DAV RIN SRM PLF VES PDF URA FMA PER CER MBU SCC GYT

(b)

e_{S222} (atom cm^{-2} s^{-1})

1460 1400 271 95 53 48 45 41 40 30 30 28 23 17 16 12 9 7 2

MPE THO TUR URA BRA RIN SRM FMU GMA FMA DAV PLF PDF VES PER MBU CER SCC GYT
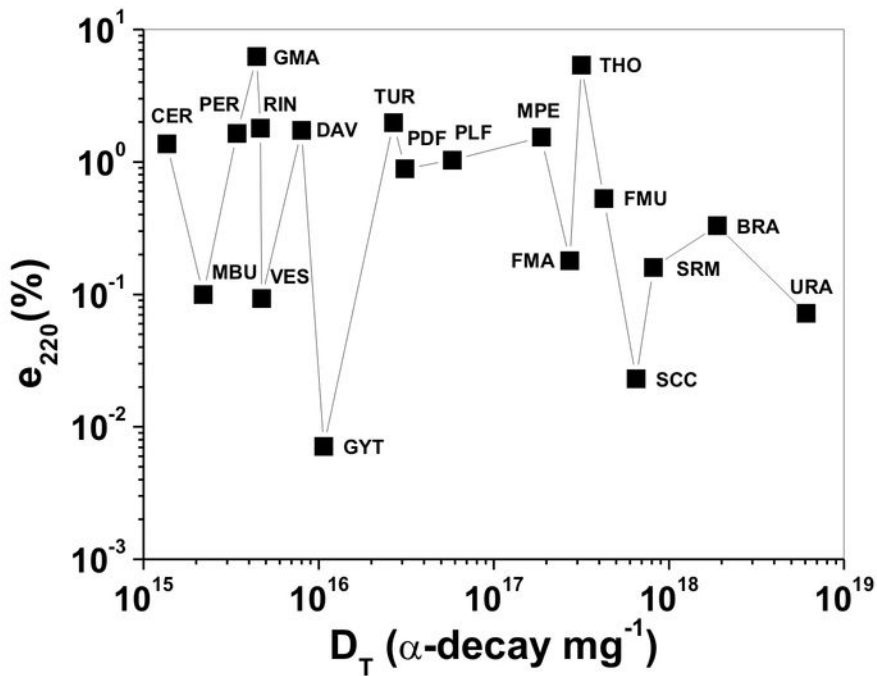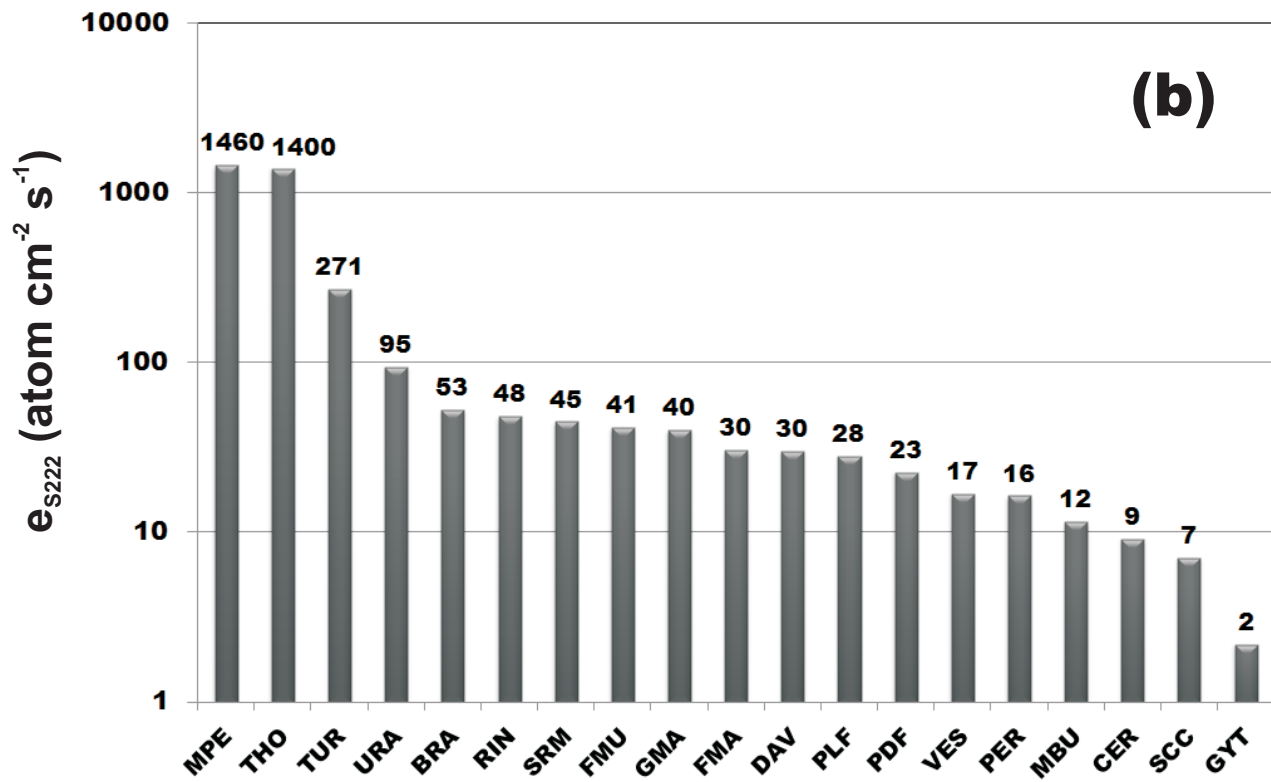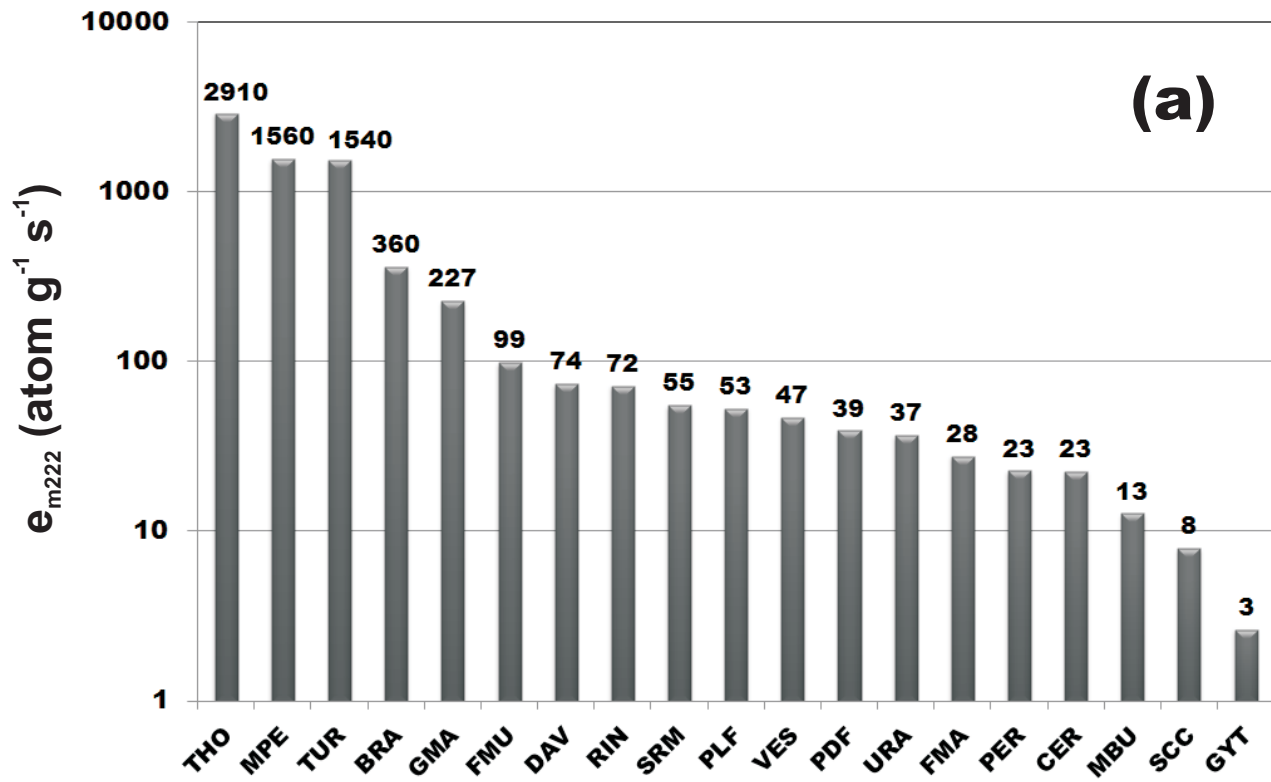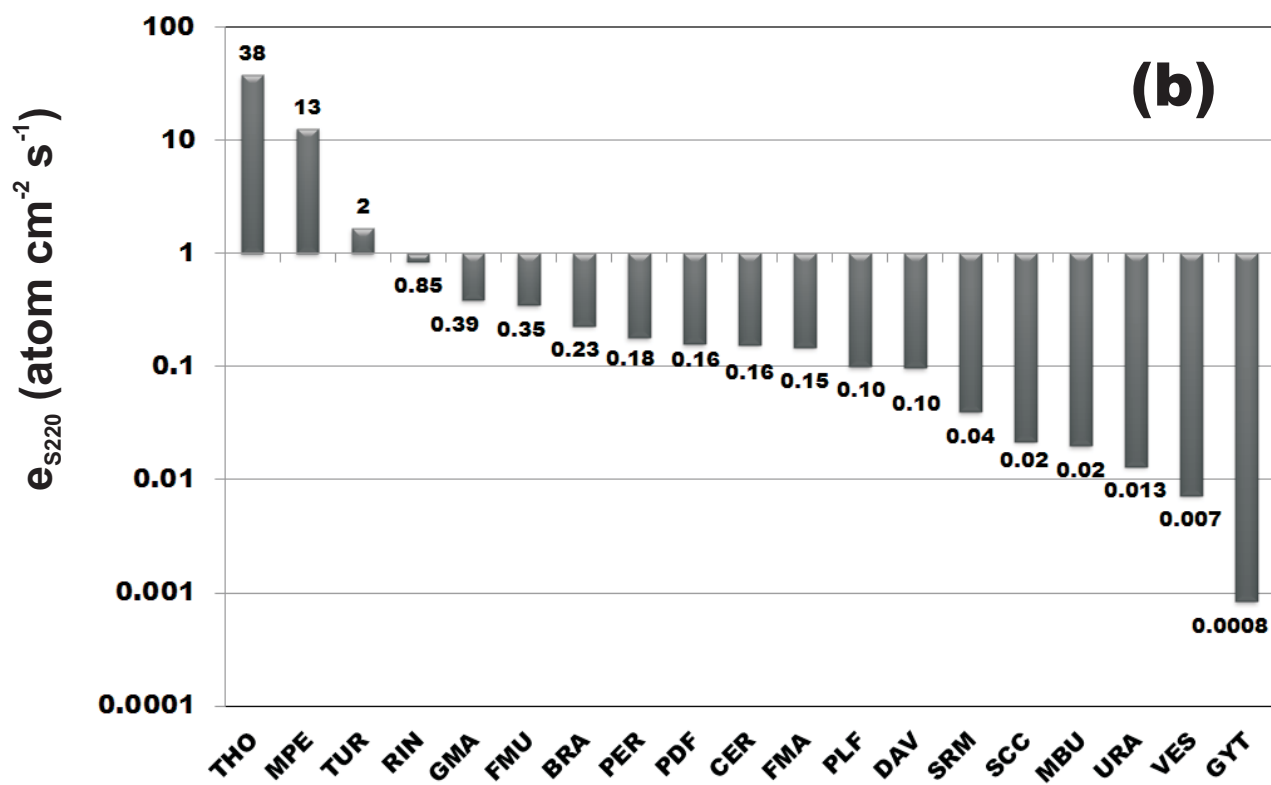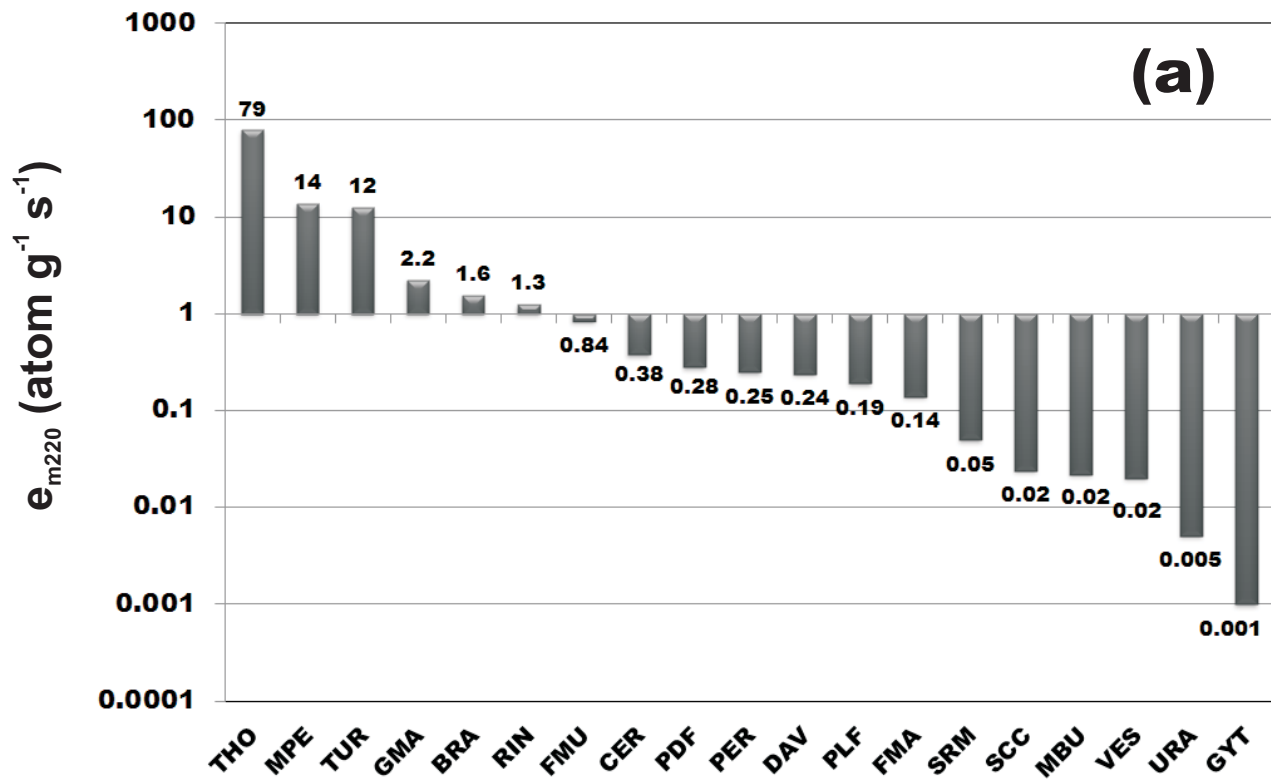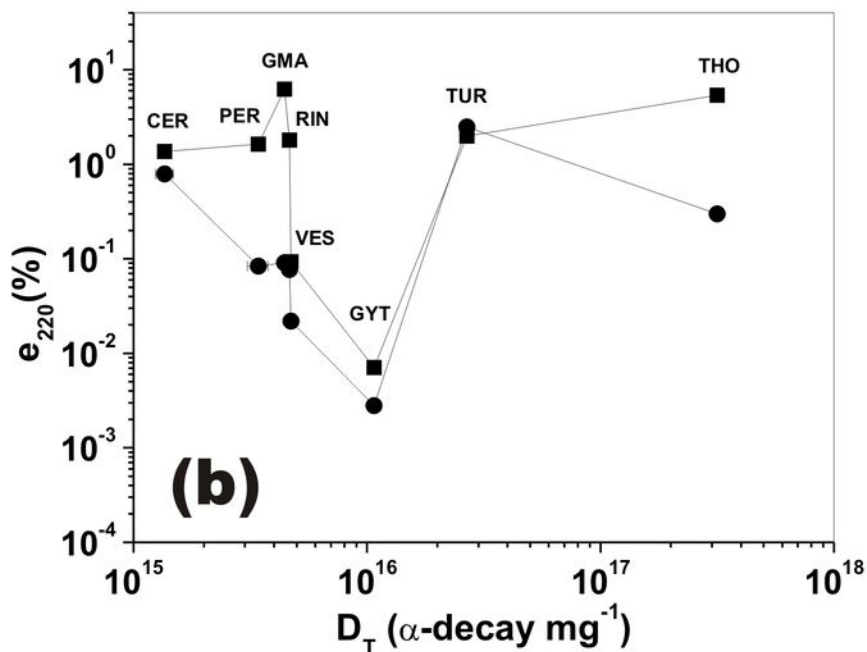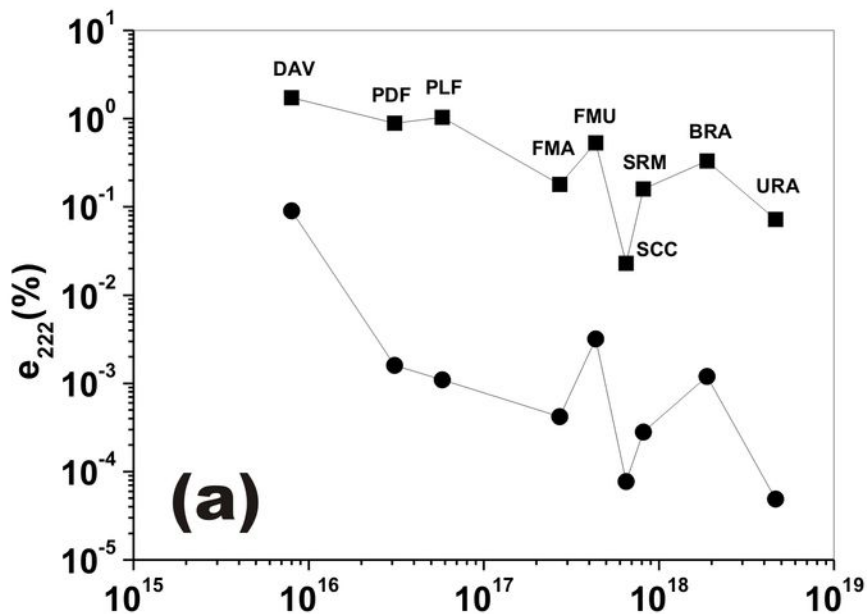
TABLE 1.

Previously reported radon emanation rates and coefficients for metamict minerals and uranium ores as measured at room temperature.

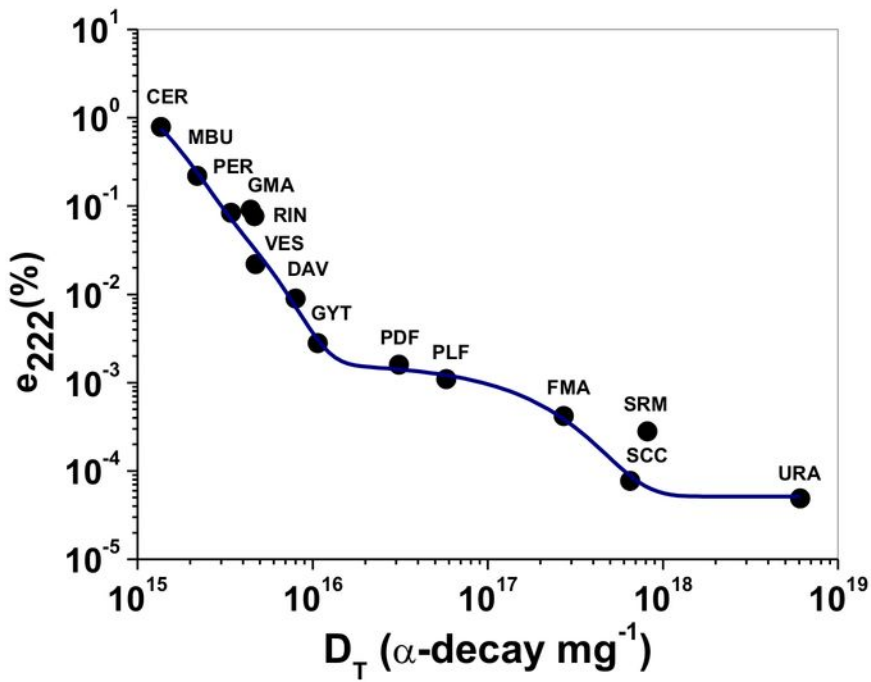| Mineral*	Fraction (μm)	^{226}Ra (Bqg^{-1})	Mean emanation rate (atoms g^{-1} min^{-1})	Emanation coefficient (%)
Cerite	< 63	42.7 ± 0.5	430 ± 1	16.8 ± 0.2
Monazite	< 63	17.6 ± 0.4	21.7 ± 0.3	2.05 ± 0.03
	1000-2000	17.6 ± 0.4	10.4 ± 0.2	0.98 ± 0.02
Thorite	< 63	104 ± 2	336.7 ± 1	5.38 ± 0.08
Uraninite	< 63	5829 ± 69	1842 ± 4	0.53 ± 0.01
	1000-2000	5829 ± 69	1860 ± 5	0.53 ± 0.01
Zircon	<63	50 ± 0.5	31.4 ± 0.2	1.04 ± 0.01
	1000-2000	50 ± 0.5	14.1 ± 0.1	0.47 ± 0.01
Uranium ore[†]				
Autunite	149-530	209-216		2-4
Carnotite	149-530	9.4-10.2		12-19
Uraninite	149-530	302-322		12-15

*Garver and Baskaran (2004).
[†] Landa (1987).

TABLE 2

Locality, U and Th activity concentrations, and ages of the samples analyzed. Sample abbreviation tags are given in parentheses next to the phase name.

Mineral	Chemical formula	Locality	^{238}U (Bqg^{-1})	^{232}Th (Bqg^{-1})	Age (10^6 year)
Oxides					
Brannerite (BRA)	UTi_2O_6	Crokers Well Granite, South Australia	3639(108)	335(4)	1579.2(15)[*]
Davidite (DAV)	$(La,Ce,Ca)(Y,U)(Ti,Fe^{3+})_{20}O_{38}$	Permian granitoid massif Bektau-Ata, Kazakhstan	103(6)	10.1(3)	251-299
Fergusonite Madawaska (FMA)	$YNbO_4$	Pegmatites, John Cole Quarry, Madawaska, Ontario, Canada	832(23)	53.9(5)	1050-1090[#]
Fergusonite Mukinbudin (FMU)		Pegmatites, Mukinbudin Quarry, Western Australia	386(12)	114(2)	2657-2675[$]
Pyrochlore (dark fraction) (PDF)	$A_{2-m}B_2X_6Y_{1-n}\cdot pH_2O$	Pegmatites, South Ural, Russia	315(8)	24.4(2)	315-375[&]
Pyrochlore (light fraction) (PLF)	A = Na, Ca, U, Th, Y, REE; B = Nb, Ta, Ti, Fe^{3+}, Zr; X=O; Y = O, OH, F; REE = rare earth elements	Pegmatites, South Ural, Russia	609(15)	13.2(1)	315-375[&]
Samarskite Centennial Cone (SCC)	ABO_4	Pegmatites, Centennial Cone, Jefferson Co., Colorado, USA	1303(50)	74.2(7)	1400-1700[†]
Samarskite Ross Mine (SRM)	A = Ca, Ti, Fe^{2+}, Fe^{3+}, REE, U, Th; B = Nb, Ta	Metamorphic rocks, Ross Mine, Yancy Co., North Carolina, USA	2503(97)	22.2(3)	1000-1200[‡]
Uraninite (URA)	UO_2	Sandstones Oklo, Gabon	9465(216)	5.1(2)	1968(50)[¥]
Phosphates					
Monazite Petaca (MPE)	$(Ce,La,Nd,Th)PO_4$	Pegmatites, Petaca, Rio Arriba Co., New Mexico, USA	26.7(8)	637(5)	1400(200)[§]
Monazite Buenopolis (MBU)		Pegmatites, Buenopolis, Minas Gerais, Brazil	0.74(4)	15.1(2)	700(35)[Σ]

Silicates

Cerite (CER)	$REE_9(Fe^{3+},Mg)(SiO_4)_6(SiO_3OH)(OH)_3$	Pegmatites, South Ural, Russia	0.36(2)	20.0(2)	315-375[&]
Gadolinite Marysin (GMA)	$REE_2Fe^{2+}Be_2Si_2O_{10}$	Pegmatites, near Szklarska Poręba, SW Poland	31.6(8)	25.8(3)	328(12)[±]
Gadolinite Ytterby (GYT)		Pegmatites, Ytterby, Sweden	12.0(4)	10.6(1)	1795(2)[≠]
Perrierite (PER)	$REE_4Fe^{2+}(Fe^{3+},Al)_2Ti_2O_8(Si_2O_7)_2$	Granitoids near Amherst, Bedford Co., Virginia, USA	3.4(3)	10.8(1)	1000-1200[‡]
Rinkite (RIN)	$(Ti,Nb,Al,Zr)(Na,Ca)_3(Ca,Ce)_4(Si_2O_7)_2(O,F)_4$	Pegmatites, Khibiny massif, Kola Peninsula, Russia	11.7(5)	50.4(5)	362(17)[£]
Thorite (THO)	$(Th,U)SiO_4$	Pegmatites, Kemp Uranium Prospect, Cardiff Twp., Canada	120(9)	1054(22)	1250-1340[@]
Turkestanite (TUR)	$Th(Ca,Na)_2(K_{1-x} \quad _x)Si_8O_{20}$	Sandy shales, Dzhelisu massif, Kyrgyzstan	7.8(4)	452(4)	299-306[€]
Vesuvianite (VES)	$Ca_{19}(Al,Mg,Fe,Ti,Mn)_{13}(B,Al,\square)_{0-5}Si_{18}O_{69}(O,OH,F)_9$	Pegmatite vein, Sludyanka, Baikal, Russia	27.3(7)	15.9(3)	447.3(24)[©]

[*] Ludwig and Cooper (1984). [#] Carr et al (2000). [$] Blight et al (1984). [&] Leech and Stockli (2000). [†] Bryant et al (1981). [‡] Mesoproterozoic age. [¥] Janeczek et al (1996). [§] Garver and Baskaran (2004). [Σ] Lumpkin and Ewing (1988). [±] Pin et al (1987). [≠] Romer and Smeds (1994). [£] Age of the Lovozero complex. [@] Easton (1992). [€] Kabalov et al (1998). [©] Reznitskii at al (2000)

TABLE 3.

Calculated α-doses for metamict mineral samples analyzed in this study.

Sample	D_{238} (10^{15} α-decay mg^{-1})	D_{235} (10^{15} α-decay mg^{-1})	D_{232} (10^{15} α-decay mg^{-1})	D_T (10^{15} α-decay mg^{-1})
Oxides				
BRA	1640	142	104	1886(54)
DAV	7.2	0.33	0.52	8.1(8)
FMA	244	16.3	11.2	272(9)
FMU	322	51.7	62	436(13)
PDF	28	1.3	1.6	31(3)
PLF	54	2.6	0.87	58(5)
SCC	577	49.7	23	650(78)
SRM	758	51.5	4.8	814(89)
URA	5500	589	2.00	6091(274)
Phosphates				
MPE	10.5	0.8	175	186(14)
MBU	0.14	0.008	2.0	2.2(1)
Silicates				
CER	0.032	0.002	1.3	1.36(12)
GMA	2.7	0.126	1.62	4.4(2)
GYT	6.3	0.61	3.78	10.7(3)
PER	1.0	0.07	2.3	3.4(4)
RIN	1.10	0.052	3.5	4.7(2)
THO	44	3.3	269	316(15)
TUR	0.61	0.028	26.2	26.8(5)
VES	3.19	0.16	1.37	4.7(1)

Doses were calculated as: $D_{238} = 8 \times N_{238}(e^{t\lambda_{238}} - 1)$, $D_{235} = 7 \times N_{235}(e^{t\lambda_{235}} - 1)$, $D_{232} = 6 \times N_{232}(e^{t\lambda_{232}} - 1)$ and $D_T = D_{238} + D_{235} + D_{232}$. N_{238}, N_{235} and N_{232} are the present number of atoms of ^{238}U, ^{235}U and ^{232}Th per milligram, λ_{238}, λ_{235} and λ_{232} are the decay constants of ^{238}U, ^{235}U and ^{232}Th (respectively), and t is the geologic age. The absorbed ^{235}U α-doses were calculated assuming a natural atomic abundance of $^{238}U/^{235}U$ = 137.88.

TABLE 4.

Total emission rates, mass and surface emanation rates, and ^{222}Rn and ^{220}Rn emanation coefficients for the metamict minerals analyzed.

Sample	N_{222} (10^7 atom s^{-1})	E_{222} (atom s^{-1})	e_{m222} (atom s^{-1} g^{-1})	e_{s222} (atom s^{-1} cm^{-2})	e_{222} (%)	N_{220} (10^3 atom s^{-1})	E_{220} (atom s^{-1})	e_{m220} (atom s^{-1} g^{-1})	e_{s220} (atom s^{-1} cm^{-2})	e_{220} (%)
Oxides										
BRA	69	143	360	53	0.0012	11.1	0.62	1.56	0.23	0.33
DAV	5.65	85.2	73.9	30.2	0.009	0.97	0.28	0.24	0.098	1.73
FMA	689	478	27.6	30.4	0.00042	77.8	2.4	0.14	0.15	0.18
FMU	20.8	112	98.9	41.4	0.0032	10.8	0.95	0.84	0.35	0.53
PDF	83.4	218	39.2	22.6	0.0016	10.4	1.55	0.28	0.16	0.89
PLF	73.7	135	52.9	28.2	0.0011	2.8	0.48	0.19	0.1	1.03
SCC	828	106	7.91	7.07	0.000077	82.5	0.32	0.024	0.022	0.023
SRM	292	136	55.4	44.8	0.00028	4.53	0.12	0.05	0.04	0.16
URA	72400	5900	36.8	94.8	0.000049	68.3	0.82	0.005	0.0132	0.072
Phosphates										
MPE	8.32	10200	1560	1460	0.74	347	89.3	13.7	12.8	1.54
MBU	0.15	54.6	12.7	11.5	0.22	5.4	0.094	0.022	0.02	0.10
Silicates										
CER	0.156	205	22.5	9.17	0.79	15.2	3.48	0.38	0.156	1.37
GMA	85.9	130	227	40.1	0.091	1.23	1.28	2.24	0.39	6.24
GYT	6	27.7	2.64	2.19	0.0028	9.28	0.011	0.001	0.00084	0.0071
PER	0.61	85.2	22.7	16.4	0.084	3.37	0.92	0.25	0.18	1.64
RIN	2.12	274	71.8	48.2	0.077	16	4.8	1.26	0.85	1.80
THO	32.1	16300	2910	1400	0.30	493	442	78.7	37.7	5.38
TUR	0.091	377	1540	207	2.49	9.19	3.03	12.4	1.67	1.98
VES	1.27	45.8	47	16.9	0.022	1.29	0.02	0.02	0.0073	0.093

TABLE 5.

Correlation matrix for ^{222}Rn and ^{220}Rn emanations and α-dose parameters from metamict oxides.

	D_{238}	D_{232}	D_T	e_{m222}	e_{s222}	e_{222} (%)	e_{m220}	e_{s220}
D_{232}	0.02							
D_T	1.00	0.03						
e_{m222}	0.08	0.87	0.09					
e_{s222}	0.92	0.12	0.92	0.23				
e_{222} (%)	-0.33	-0.06	-0.33	0.07	-0.19			
e_{m220}	-0.06	0.94	-0.04	0.94	0.12	0.11		
e_{s220}	-0.35	0.69	-0.34	0.49	-0.13	0.21	0.75	
e_{220} (%)	-0.45	-0.25	-0.46	-0.02	-0.33	0.85	0.01	0.13

TABLE 6.

Correlation matrix for ^{222}Rn and ^{220}Rn emanations and α-dose parameters from metamict silicates.

	D_{238}	D_{232}	D_T	e_{m222}	e_{s222}	e_{222} (%)	e_{m220}	e_{s220}	e_{220} (%)
D_{232}	0.98								
D_T	0.99	1.00							
e_{m222}	0.84	0.91	0.90						
e_{s222}	0.97	1.00	1.00	0.93					
e_{222} (%)	-0.14	0.00	-0.02	0.38	0.04				
e_{m220}	0.97	1.00	1.00	0.94	1.00	0.06			
e_{s220}	0.99	1.00	1.00	0.89	1.00	-0.05	0.99		
e_{220} (%)	0.52	0.55	0.55	0.55	0.57	-0.02	0.57	0.56	